Spin-based effects and transport properties of a spin-orbit-coupled hexagonal optical lattice

G.-B. Zhu,[1,2] Q. Sun,[1,3] Y.-Y. Zhang,[4,5] K. S. Chan,[2] W.-M. Liu,[3] and A.-C. Ji[1,*]

[1]*Department of Physics, Capital Normal University, Beijing 100048, China*

[2]*Department of Physics and Materials Science, City University of Hong Kong, Tat Chee Avenue, Kowloon, Hong Kong, China*

[3]*Institute of Physics, Chinese Academy of Sciences, Beijing 100190, China*

[4]*SKLSM, Institute of Semiconductors, Chinese Academy of Sciences, P.O. Box 912, Beijing 100083, China*

[5]*ICQM, Peking University, Beijing 100871, China*

(Received 21 January 2013; revised manuscript received 30 July 2013; published 13 August 2013)

We investigate an ultracold Fermi gas in a hexagonal lattice subjected to a strong Rashba spin-orbit coupling (SOC). We focus on the marginal Abelian limit with the strength of SOC $\kappa = \pi/2$, where the derived Dirac fermions are spin-1/2 spinors in contrast to the pure hexagonal lattice. We find a double-degeneracy at the center of the Brillouin zone, which is a spin-3/2 Dirac-Weyl fermion that can be represented as two spin-1/2 fermions. While at the corner of the Brillouin zone, there occur another two spin-1/2 fermions. These Dirac spinors display a verity of spin textures beyond the usual topological properties. Furthermore, we investigate the energy spectrum of one-dimensional (1D) zigzag and armchair ribbons, and show that the appearance of a new cone at the center of the Brillouin zone can induce two flat bands in a 1D zigzag ribbon. These unique properties allow us to transport a single spin-1/2 Dirac spinor through the 1D zigzag ribbon with two quasi-two-dimensional leads, where only the spin-up or spin-down freedom of the Dirac spinors can transit through the ribbon.

DOI: 10.1103/PhysRevA.88.023608 PACS number(s): 67.85.Lm, 05.30.Fk, 37.10.Jk, 71.10.Fd

I. INTRODUCTION

The successful control of ultracold atoms in optical lattices has made it an ideal playground to explore a variety of fascinating quantum phenomena [1]. One example is that the two-dimensional (2D) hexagonal optical lattice has attracted considerable interest both theoretically [2–4] and experimentally [5,6]. The artificial honeycomb geometry can give rise to Dirac cones, such as that of graphene [7], which are of great importance in the study of remarkable behaviors of relativistic fermions.

More recently, spin-orbit coupling (SOC) has become an exciting forefront [8,9] because of its potential application in future spintronics [10,11]. This has motivated much effort in creating artificial non-Abelian gauge fields in ultracold atoms [12], where both the spin-orbit-coupled Bose-Einstein condensate [13] and Fermi gas [14,15] have been successfully realized. Such advances open up a new avenue towards exploring many novel physics of an optical lattice subjected to SOC [16–21]. Especially, it was shown that the emerging relativistic fermions can also occur in a square lattice, where the strong Rashba SOC plays the key role [16].

However, although the above relativistic fermions have attracted great attention and have been discussed many times in both the solid-state and ultracold-atom communities, the degrees of freedom of the real and pseudo spins are not involved simultaneously. Therefore, it is natural to study a new system by combining the strong SOC of Ref. [16] with a honeycomb geometry. In contrast to graphene, when a fermion hops between two honeycomb sublattices, the accompanying spin will be flipped.

In this paper, we focus on the marginal Abelian limit with the strength of SOC $\kappa = \pi/2$, where the emerging Dirac fermions become spin-1/2 spinors. We show that there occurs a spin-3/2 Dirac-Weyl fermion at the center of the Brillouin zone, which can be represented as two spin-1/2 fermions. While at the corner of the Brillouin zone, another two spin-1/2 fermions occur. In contrast to the well-studied pure hexagonal lattice, these Dirac spinors display a variety of spin textures beyond the usual topological properties. Furthermore, because the mesoscopic property is of great interest in honeycomb geometry, we also investigate the energy spectrum of one-dimensional (1D) zigzag and armchair ribbons. We demonstrate that the appearance of a new cone at the center of the Brillouin zone can induce two flat bands in a 1D zigzag ribbon, which is of significance for mesoscopic transports. Finally, we calculate the transport conductance of the 1D zigzag ribbon with two quasi-2D leads, and we find that only the spin-up or spin-down freedom of the Dirac spinors can transit through the zigzag ribbon.

This paper is organized as follows: We first discuss the single-particle spectrum of the system in Sec. II. Then in Sec. III, we derive the effective Hamiltonians at the center and corner of the Brillouin zone. In Sec. IV, we analyze the topological properties and spin configurations of the effective Hamiltonians. After that, we investigate the energy spectrum of 1D zigzag and armchair ribbons in Sec. V, and calculate the conductance of the 1D zigzag ribbon with two quasi-2D leads in Sec. VI. Finally, the experimental feasibility of the actual realization of the effective models is discussed in Sec. VII.

II. MODEL OF SPIN-ORBIT-COUPLED HEXAGONAL OPTICAL LATTICE AND ENERGY SPECTRUM

We consider a system of two-component fermionic atoms moving in a two-dimensional optical potential V_{OL}. In the noninteracting limit, which can be obtained by means of Feshbach resonances [22], the Hamiltonian of the system can

*andrewjee@sina.com

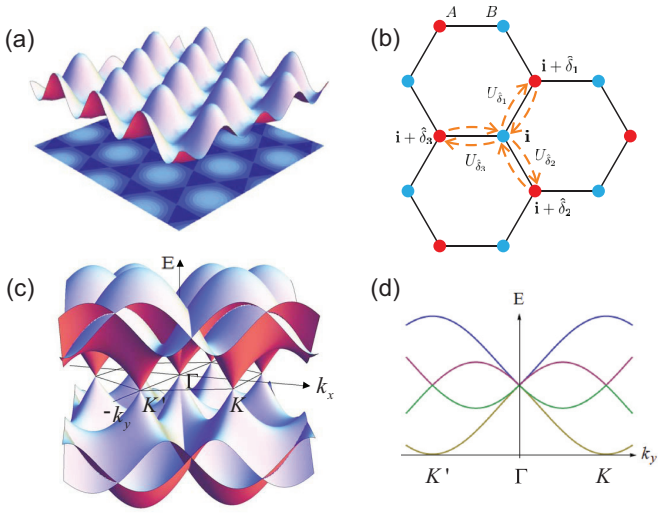

FIG. 1. (Color online) Hexagonal lattice and single-particle energy spectrum. (a) Optical lattice potential $V_{\rm OL}$ and the contour, where a hexagonal lattice is made out of the minima of the potentials. (b) Lattice structure with A and B denoting two sublattices, where $\hat{\delta}_j, j = 1,2,3$ are the nearest neighbor vectors, and $U_{\hat{\delta}}$ represent the non-Abelian tunneling matrices. (c) Energy band structure of the hexagonal lattice in the marginal Abelian regime, where a new Dirac cone appears at the center of the Brillouin zone Γ in addition to K, K' cones. (d) Dispersion of the energy spectrum along k_y axis with $k_x = 0$. Note that while the bands at K, K' become nondegenerate, there exhibits an extra double degeneracy around Γ.

be described by

$$H = \int \psi^\dagger \left[\frac{1}{2m}(\vec{k}^2 + 2\kappa \vec{k}\cdot\vec{\tau}) + V_{\rm OL} \right] \psi \, dx\, dy, \qquad (1)$$

where $\psi = (\psi_\uparrow, \psi_\downarrow)^T$ is the two-component fermionic field operator, κ is the strength of Rashba SOC and $\vec{\tau} = \{\tau_x, \tau_y\}$, where $\tau_{x,y}$ are the spin Pauli matrices. The optical potential can be given by $V_{\rm OL} = \sum_{j=1,2,3} V \cos^2[k_L(x\cos\theta_j + y\sin\theta_j)]$ with $\theta_1 = \pi/3, \theta_2 = 2\pi/3, \theta_3 = 0$, and $k_L = \pi/a$ (a is the lattice spacing) [2], where the minima of $V_{\rm OL}$ form a hexagonal lattice, as shown in Fig. 1(a). The above Hamiltonian can be rewritten in a gauge-field form, which reads

$$H = \int \hat{\psi}^\dagger \left[\frac{1}{2m}(\vec{k} + \vec{A})^2 + V_{\rm OL} \right] \hat{\psi} \, dx\, dy, \qquad (2)$$

with $\vec{A} = \kappa(\tau_x, \tau_y)$ being the non-Abelian gauge-field induced by Rashba SOC. Then, in the deep optical lattice limit, we can use the Wannier functions expansion and derive the tight-binding model

$$H = -t \sum_{\mathbf{i}} \sum_{\hat{\delta}} [\psi^\dagger_{\mathbf{i}+\hat{\delta}} U_{\hat{\delta}} \psi_{\mathbf{i}} + \text{H.c.}], \qquad (3)$$

where t is the overall hopping amplitude, $\psi^\dagger_{\mathbf{i}} = (c^\dagger_{\mathbf{i}\uparrow}, c^\dagger_{\mathbf{i}\downarrow})$ with $c^\dagger_{\mathbf{i}\uparrow(\downarrow)}$ the creation operator for spin-up (down) fermion at site $\mathbf{i}$. $\hat{\delta}$ are the nearest neighbor vectors of the hexagonal lattice, which are given by $\hat{\delta}_1 = \frac{a}{2}(1, \sqrt{3})$, $\hat{\delta}_2 = \frac{a}{2}(1, -\sqrt{3})$, and $\hat{\delta}_3 = a(-1, 0)$ (a is the lattice spacing), see Fig. 1(b). The nearest sites tunneling matrices are $U_{\hat{\delta}} = e^{i\vec{A}\cdot\hat{\delta}}$ with $\vec{A} = \kappa(\tau_x, \tau_y)$ the non-Abelian gauge-field induced by Rashba SOC [16–18]. Here, the diagonal terms of $U_{\hat{\delta}} = \cos\kappa \hat{I} + i \sin\kappa \, (\vec{\tau}\cdot\hat{\delta})$ denote the spin-conserved hopping, while the off-diagonal terms describe the spin-flipped hopping, which is induced by the above Rashba-type non-Abelian gauge field.

Then, in the momentum space, we have the following Hamiltonian on the basis of the four-component wave function $\Psi = (\psi_{A\uparrow}, \psi_{A\downarrow}, \psi_{B\uparrow}, \psi_{B\downarrow})^T$:

$$H(\vec{k}) = \begin{pmatrix} m + \Delta & 0 & u(\vec{k}) & v_1(\vec{k}) \\ 0 & m - \Delta & v_2(\vec{k}) & u(\vec{k}) \\ u^*(\vec{k}) & v_2^*(\vec{k}) & -m + \Delta & 0 \\ v_1^*(\vec{k}) & u^*(\vec{k}) & 0 & -m - \Delta \end{pmatrix}, \qquad (4)$$

with the matrix elements $u(\vec{k}) = -t\cos\kappa \sum_{\vec{\delta}} e^{i\vec{k}\cdot\vec{\delta}}$, $v_1(\vec{k}) = -it\sin\kappa \sum_{\vec{\delta}} e^{i\vec{k}\cdot\vec{\delta}} (\vec{\delta}\cdot\vec{\tau})_{\uparrow\downarrow}$, and $v_2(\vec{k}) = -it\sin\kappa \sum_{\vec{\delta}} e^{i\vec{k}\cdot\vec{\delta}} (\vec{\delta}\cdot\vec{\tau})_{\downarrow\uparrow}$. Here, we have also included a staggered sublattice potential m [23] and a polarization field Δ which introduces the population imbalance between two fermionic components. The corresponding energy spectrum of the Hamiltonian [Eq. (4)] can be obtained as

$$E^2(\vec{k}) = |u|^2 + \frac{|v_1|^2 + |v_2|^2}{2} + m^2 + \Delta^2 \pm \sqrt{\left[\frac{|v_1|^2 - |v_2|^2}{2}\right]^2 + |u|^2(|v_1|^2 + |v_2|^2) + u^2 v_1^* v_2^* + u^{*2} v_1 v_2 + 4\Delta^2(|u|^2 + m^2) + 2m\Delta(|v_1|^2 - |v_2|^2)}. \qquad (5)$$

We now discuss the peculiar properties of the corresponding energy bands of Eq. (5). For simplicity, here we consider the case with both m and Δ being zero. First for $\kappa = 0$, the band structure is explicitly as that of graphene where the Dirac cones at K, K' are spin degenerate. However, when the SOC is added to the lattice, both the up and down spin components will be mixed, and each of the spin degenerate band would be split into two Rashba bands. Specifically, in the vicinity of $\kappa = \pi/2$ where the spin-flipped process dominates, the Wilson loop characterized by $W = \text{tr}[U_{\hat{\delta}_1} U_{\hat{\delta}_2} U_{\hat{\delta}_3} U^\dagger_{\hat{\delta}_1} U^\dagger_{\hat{\delta}_2} U^\dagger_{\hat{\delta}_3}]$ reduces to the marginal Abelian regime with $|W| = 2$ [16]. In this case, there develops a significant new cone at the center of the Brillouin zone beyond the two familiar K, K' cones of graphene [see Fig. 1(c)]. Interestingly, we find that while the energy bands around K, K' are nondegenerate, the bands around the Γ point exhibit an extra two-fold degeneracy, as shown in Fig. 1(d). The general case with nonzero m and Δ will be discussed below.

III. EFFECTIVE HAMILTONIAN AND EIGENVECTORS NEAR Γ AND K, K' POINTS

To gain more insight into the above results around Γ and K, K' points, it is instructive to derive the effective low-energy Hamiltonian in the marginal Abelian regime with $\kappa = \pi/2$. We first consider the Γ point, the effective Hamiltonian reads (see Appendix A)

$$H_\Gamma = \tfrac{3}{2}\vec{\alpha}\cdot\vec{k} + m\beta + \Delta\hat{I}_\sigma \otimes \tau_z, \tag{6}$$

where $\vec{\alpha} = \sigma_x \otimes \tau_i$ with σ_i, $i = x, y$ being the Pauli matrices representing the AB-sublattice pseudo-spin degrees of freedom and $\beta = \sigma_z \otimes \hat{I}_\tau$.

At first sight, when $\Delta = 0$, Eq. (6) bears the same form of the archetype four-component Dirac fermion with $k_z = 0$ [24]. However, as is well known, the archetype Dirac fermion can only appear in $3+1$ dimensions, but in the case of $2+1$ dimensions it suffices to use 2×2 matrices to define the Clifford algebra [25,26]. Actually, the double degeneracy at Γ point shows that this is a spin-3/2 Dirac-Weyl fermion that can be represented as two spin-1/2 fermions [25]. In Appendix A, we see that the two positive-energy wave functions are in fact spin-1/2 spinors with $u_1 = (\cos\frac{\theta_+}{2}e^{-i\varphi_{\vec{k}}}, \sin\frac{\theta_+}{2})^T$ and $u_2 = (\sin\frac{\theta_-}{2}, \cos\frac{\theta_-}{2}e^{i\varphi_{\vec{k}}})^T$, in the spin subspace $(\psi_{A\uparrow}, \psi_{B\downarrow})^T$ and $(\psi_{B\uparrow}, \psi_{A\downarrow})^T$, respectively. Here, $\cos\theta_\pm = \frac{m\pm\Delta}{\sqrt{\frac{9}{4}k^2+(m\pm\Delta)^2}}$ and $\varphi_{\vec{k}} = \arctan\frac{k_y}{k_x}$. Generally, Eq. (6) can be decoupled into two effective Hamiltonians $H_\Gamma^1 = \frac{3}{2}(k_x\tau_x + k_y\tau_y) + (m+\Delta)\tau_z$ and $H_\Gamma^2 = \frac{3}{2}(k_x\tau_x + k_y\tau_y) - (m-\Delta)\tau_z$ for the two spin-1/2 Dirac spinors, respectively.

While for the K and K' points, the corresponding effective Hamiltonians $H_{K(K')}$ and eigenvectors $U_{K(K')}$ are also given in Appendix A. We find that the nonzero positive-energy wave functions of $H_{K(K')}$ are spin-1/2 spinors with $u_K = (\sin\frac{\theta_-}{2}, \cos\frac{\theta_-}{2}e^{-i\varphi_{\vec{k}}})^T$ and $u_{K'} = (\cos\frac{\theta_+}{2}e^{i\varphi_{\vec{k}}}, \sin\frac{\theta_+}{2})^T$ in the spin subspace $(\psi_{A\uparrow}, \psi_{B\downarrow})^T$ and $(\psi_{B\uparrow}, \psi_{A\downarrow})^T$, respectively. Significantly, note that $u_{K(K')}$ are complex conjugate to $u_{2(1)}$ with the same eigenenergies, and we arrive at the following effective Hamiltonians for the two spin-1/2 Dirac spinors at K, K' points: $H_K = \frac{3}{2}(-k_x\tau_x + k_y\tau_y) - (m-\Delta)\tau_z$ and $H_{K'} = \frac{3}{2}(-k_x\tau_x + k_y\tau_y) + (m+\Delta)\tau_z$.

We then discuss the roles of parameters m and Δ in the effective Hamiltonians. First for $m \neq 0, \Delta = 0$ or $\Delta \neq 0, m = 0$, $u_{1,2}$ are still double degenerate but open the same gaps as the other two spin-1/2 fermions $u_{K,K'}$. While for the general case with both m and Δ, the double degeneracy would be broken, the $u_1 - u_{K'}$ branches open a large gap $m+\Delta$ and the $u_2 - u_K$ branches possess a small gap $|m-\Delta|$. In this work, we assume that both m and Δ are positive.

IV. TOPOLOGICAL PROPERTIES AND SPIN CONFIGURATIONS OF THE EFFECTIVE HAMILTONIANS

Now, we discuss the topological properties of the spin-1/2 Dirac fermions of the effective Hamiltonians $H_\Gamma^{1(2)}$ and $H_{K(K')}$. The Berry curvatures are calculated through $\Omega_\gamma = \langle\partial_{k_x}u_\gamma|\partial_{k_y}u_\gamma\rangle - \langle\partial_{k_y}u_\gamma|\partial_{k_x}u_\gamma\rangle$. Here, u_γ represents the positive-energy branches of $u_{1(2)}$ or $u_{K'(K)}$. Then, the Chern number of each branch is given by $\mathcal{C}_{u_\gamma} = \frac{1}{2\pi}\int d^2k\Omega_\gamma$, see Fig. 2.

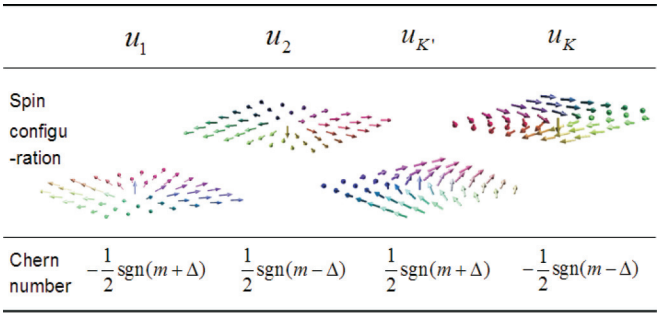

FIG. 2. (Color online) Spin configurations and Chern numbers for the positive-energy branches $u_{1(2)}$ and $u_{K'(K)}$. Here, the spin textures are for $m > \Delta$.

First, for the case $m \neq 0$ but $\Delta = 0$, both the time-reversal symmetries of $H_\Gamma^{1(2)}$ and $H_{K(K')}$ are conserved. The Chern number of the two degenerate branches $u_{1(2)}$ reads $C_{u_{1(2)}} = \mp\frac{1}{2}\mathrm{sgn}\, m$, which gives rise to the zero Chern number at Γ point, i.e., $\mathcal{C}_\Gamma = C_{u_1} + C_{u_2} = 0$. This means that there is no anomalous charge Hall conductivity for Γ point. On the other hand, because each branch bears spin freedom as shown below, the Berry curvature induces a spin Hall conductivity $\sigma_\Gamma^s = (C_{u_1} - C_{u_2})/h = -1/h$. The same analysis can be applied to $u_{K'(K)}$ and we derive $\mathcal{C}_{u_{K'(K)}} = \pm\frac{1}{2}\mathrm{sgn}\, m$. We see that the total Chern number at K, K' points vanishes $\mathcal{C}_{K-K'} = C_{u_{K'}} + C_{u_K} = 0$, but with a nonzero $\sigma_{K-K'}^s = (C_{u_{K'}} - C_{u_K})/h = 1/h$. However, due to the time-reversal symmetry of the system, the sum of the Chern numbers $\mathcal{C}_{\mathrm{sum}} = \mathcal{C}_\Gamma + \mathcal{C}_{K-K'}$ and the spin Hall conductivity $\sigma_{\mathrm{sum}}^s = \sigma_\Gamma^s + \sigma_{K-K'}^s$ at Γ and K, K' points all vanish.

While for the another case with nonzero Δ but $m = 0$, both the time-reversal symmetries of $H_\Gamma^{1(2)}$ and $H_{K(K')}$ are broken by Δ. In such a situation, we have $C_{u_{1(2)}} = -\frac{1}{2}\mathrm{sgn}\,\Delta$, which give rise to a nonzero Chern number at Γ point with $\mathcal{C}_\Gamma = -1$. This is similar to Haldane's model for a quantum-hall insulator without Landau levels [27]. Similarly, we have $\mathcal{C}_{u_{K'(K)}} = \frac{1}{2}\mathrm{sgn}\,\Delta$ and $\mathcal{C}_{K-K'} = 1$ for K, K' points. Here we should mention that, although the time-reversal symmetry breaking produces nonzero Chern numbers at Γ and K, K' points, the overall Chern number $\mathcal{C}_{\mathrm{sum}} = 0$ *due to the important fact that* $u_{K(K')}$ *are complex conjugate to* $u_{2(1)}$. As to the spin Hall conductivity, we have $\sigma_\Gamma^s = \sigma_{K-K'}^s = 0$.

Finally, for the general situation with both m and Δ, we derive the corresponding Chern number $\mathcal{C}_{u_{1(K')}} = \mp\frac{1}{2}\mathrm{sgn}(m+\Delta)$ and $\mathcal{C}_{u_{2(K)}} = \pm\frac{1}{2}\mathrm{sgn}(m-\Delta)$. We see that either for $m > \Delta$ or $m < \Delta$, the overall Chern number $\mathcal{C}_{\mathrm{sum}}$ and spin Hall conductivity σ_{sum}^s are zero. Therefore, although the topological properties of each 1/2-spinor are nontrivial, there is no topological order in the overall system and no topological phase transitions occur. Furthermore, the above Chern numbers can also be calculated by

$$\mathcal{C}_{u_\gamma} = \frac{1}{4\pi}\int d^2k\left(\partial_{k_x}\vec{h}^\gamma \times \partial_{k_y}\vec{h}^\gamma\right)\cdot\vec{h}^\gamma, \tag{7}$$

with $\vec{h}^\gamma$ representing the projection of $H_\Gamma^{1(2)}$ and $H_{K(K')}$ into the spin subspaces spanned by (τ_x, τ_y, τ_z). Then, we obtain

$\vec{h}^{1(K')} = (\sin\theta_+\cos\varphi_{\vec{k}}, \pm\sin\theta_+\sin\varphi_{\vec{k}}, \cos\theta_+)$, $\vec{h}^{2(K)} = (\sin\theta_-\cos\varphi_{\vec{k}}, \pm\sin\theta_-\sin\varphi_{\vec{k}}, -\cos\theta_-)$, respectively. In fact, $\vec{h}^{\gamma}$ represents the real spin configurations in the spin subspaces, see Fig. 2. The corresponding topological structures are defined by plotting $\vec{h}^{\gamma}$ as a function of $\vec{k}$. We find that they can be visualized by the meron configurations of vectors $\vec{h}^{\gamma}$. The meron is a half skyrmion, where it points to the north (or the south) pole at the origin and winds around the equator at the boundary with $\pm 1/2$ topological charge [28]. This can be clearly seen in the s_z value of spin $\vec{s} = \frac{\vec{\tau}}{2}$ with $s_z^{\gamma} = h_z^{\gamma}$, which gives rise to $s_z^{1(K')} = \cos\theta_+/2$ and $s_z^{2(K)} = -\cos\theta_-/2$. By the definition $\cos\theta_\pm = \frac{m\pm\Delta}{\sqrt{\frac{9}{4}k^2+(m\pm\Delta)^2}}$, we have $\cos\theta_\pm = \pm 1$ at the center of each cone with $k = 0$, depending on the sign of $m \pm \Delta$. Therefore, each branch is the s_z spin eigenstate at the center of the cones, while s_z^{γ} vanishes away from the center. In Fig. 2, both the topological properties and spin configurations of each band are entirely determined by the two external parameters m and Δ.

V. SPECTRUM OF ZIGZAG AND ARMCHAIR RIBBONS

In this section, we investigate the mesoscopic behaviors of the system. As is well known, the central issue regarding graphene is how it behaves when it is patterned at the nanometer scale with different edge geometries, i.e., the ribbons. Such ribbons with various types of edges have been shown to exhibit dramatically different properties [29–31]. Here, we calculate the energy spectrum of 1D zigzag and armchair ribbons in the marginal Abelian limit with $\kappa = \pi/2$. We note that because the unique properties of the system arise from the combination of the strong non-Abelian gauge field and honeycomb geometry of the optical lattice, the edges also play important roles.

For the 1D ribbon with zigzag (armchair) edges, the Hamiltonian is translation invariant along the x (y) direction. The corresponding configuration of the ribbon is depicted in Fig. 1 of Ref. [30]. We assume that there are N A-type and NB-type atoms in a unit cell. Then, the corresponding tight-binding Hamiltonian can be represented as

$$H_{z,a} = \hat{\phi}^{\dagger}\begin{pmatrix} 0 & T_{z,a}^{\text{intra}} & 0 & \left(T_a^{\text{inter}}\right)^* & \cdots \\ \left(T_{z,a}^{\text{intra}}\right)^{\dagger} & 0 & T_{z,a}^{\text{inter}} & 0 & \cdots \\ 0 & \left(T_a^{\text{inter}}\right)^{\dagger} & 0 & T_{z,a}^{\text{intra}} & \cdots \\ \left(\left(T_a^{\text{inter}}\right)^*\right)^{\dagger} & 0 & \left(T_{z,a}^{\text{intra}}\right)^{\dagger} & 0 & \cdots \\ \cdots & \cdots & \cdots & \cdots & \cdots \end{pmatrix}\hat{\phi},$$

where $\hat{\phi} = [c_{1A\uparrow}, c_{1A\downarrow}, c_{1B\uparrow}, c_{1B\downarrow}, \ldots, c_{NA\uparrow}, c_{NA\downarrow}, c_{NB\uparrow}, c_{NB\downarrow}]$ and z, a denote the zigzag and armchair ribbons, respectively. $T_{z,a}^{\text{intra,inter}}$ represents the intracell and intercell hopping matrix in the 1D momentum space, see Appendix B. By diagonalizing the Hamiltonian $H_{z,a}$, we can derive the corresponding energy spectrum of the SO-coupled ribbons. Figure 3 shows the results for $m = \Delta = 0$. We find that while there are no edge states for the armchair case similar to graphene, the behaviors of edge states in the zigzag ribbon are dramatically changed by the SOC. Significantly, the appearance of the new cone at Γ in Fig. 1(c) induces two flat bands, which connect the $u_1 - u_{K'}$ and $u_2 - u_K$ energy bands.

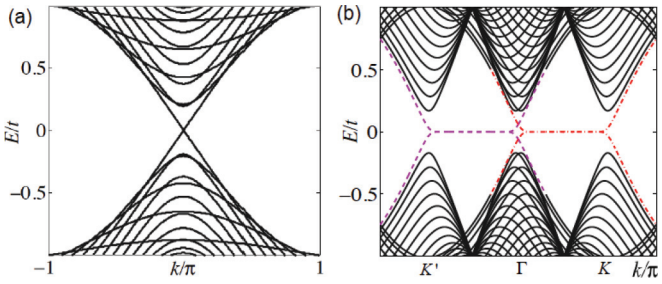

FIG. 3. (Color online) Energy dispersion of the 1D ribbons for $m = \Delta = 0$. The ribbon width $N = 26$ in a unit cell. (a) For the armchair ribbon, the SOC does not affect the behaviors of the lowest propagating mode and there are no edge states. (b) For the zigzag ribbon, there appears two flat bands connecting the $u_1 - u_{K'}$ (dashed lines) and $u_2 - u_K$ (dash-dotted lines) energy bands, respectively.

The energy spectrum of the 1D zigzag ribbon for the general situation is shown in Fig. 4(b), where for either $m > \Delta$ or $m < \Delta$, the spectra are the same, and the flat band opens up a large gap $m + \Delta$ for $u_1 - u_{K'}$ and a small gap $|m - \Delta|$ for the $u_2 - u_K$ branches. Here we should mention that because there is no topological order in this system, the flat bands come from the honeycomb geometry, such as that of graphene, which could not be confused with the edge states in the topological insulators [8]. Nevertheless, the nontrivial topological properties of each spin-1/2 spinor can be explored through the so-called valley-filter scheme [32] as shown in Sec. VI.

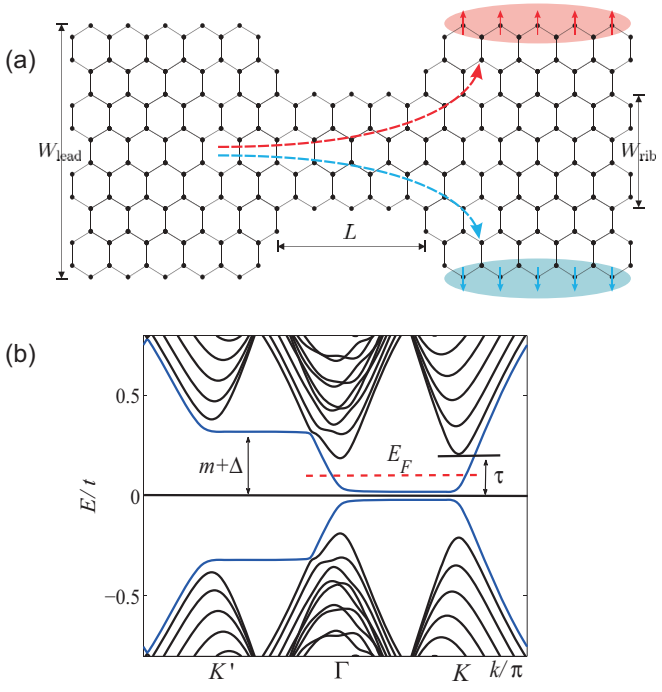

FIG. 4. (Color online) (a) Transport configuration of the 1D zigzag ribbon coupled with two quasi-2D leads. (b) Energy dispersion of the 1D zigzag ribbon contact, where the flat bands open up a large gap $m + \Delta$ for the $u_1 - u_{K'}$ branches, and the Fermi energy E_F can be tuned to lie only at the $u_2 - u_K$ positive-energy branches which possess a small gap $|m - \Delta|$. τ is the minimal energy of the first mode of u_K band.

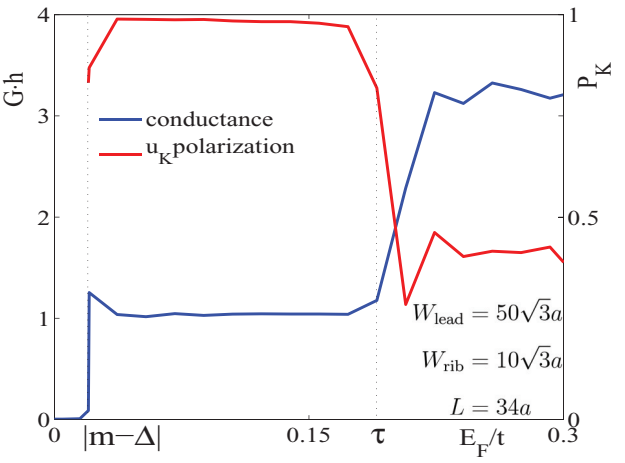

FIG. 5. (Color online) Conductance and valley polarization of u_K branch for the configuration depicted in Fig. 4(a) as a function of Fermi energy E_F. In the region $|m-\Delta| < E_F < \tau$ [see Fig. 4(b)], the conductance is quantized with $G = 1/h$ and only the u_K branch of the leads can be transmitted with $P_K \simeq 1$.

VI. CONDUCTANCE OF THE 1D ZIGZAG RIBBON WITH TWO QUASI-2D LEADS

Now, we calculate the conductance of 1D zigzag ribbon coupled with two quasi-2D leads, which may display novel spin-based transports phenomena. More recently, there have been great advances in investigating the transporting properties of ultracold gases [22,33]. Especially, the mesoscopic transport through a 1D channel has been successfully realized in experiments [34]. Here, we consider a 1D zigzag ribbon contact, which is connected to two quasi-2D leads, as depicted in Fig. 4(a). Such a configuration can be realized by separating two reservoirs of ultracold atoms through a narrow channel, which is imprinted by using two lobes of a laser beam [34].

We shall consider a general situation with the strength of SOC $\kappa = 0.98(\pi/2)$, close to the marginal Abelian regime. The polarization field is fixed to $\Delta = 0.15$, for example, while the staggered potential m is tunable. The chosen parameter range of interest is $m \sim \Delta$, where the flat bands in Fig. 3(b) would open a large gap $m + \Delta$ for $u_1 - u_{K'}$ branches and a small gap $|m - \Delta|$ for $u_2 - u_K$ branches. The Fermi energy E_F is tuned to lie at the $u_2 - u_K$ positive-energy bands. Then, the properties of ballistic transports will be determined by the 1D zigzag ribbon contact as shown in Fig. 4(b).

The conductance of the 1D zigzag ribbon can be calculated by the widely used Landauer formula $G = \frac{1}{h}\sum_{\mu=-M}^{M} T_\mu$ with $T_\mu = \sum_{\nu=-M}^{M} |t_{\mu\nu}|^2$. Here, μ is the propagating mode of the quasi-2D leads at Fermi energy E_F with $\mu = -1, -2, \ldots, -M$ lying in the u_2 branch and $\mu = 0,1,2,\ldots,M$ lying in the u_K branch [32]. Note that, the propagating zeroth mode, $\mu = 0$, comes from the flat band. The key step is then to calculate numerically the transmission matrix elements $t_{\mu\nu}$, where we have extended the method of Ref. [35] to include the SOC-induced spin-flipped hopping. To illustrate, here we take $W_{\text{lead}} = 150a$ for the width of the quasi-2D leads, $W_{\text{rib}} = 30a$ and $L = 34\sqrt{3}a$ for the width and length of the 1D ribbon, and $m = 0.17$, for example.

Figure 5 shows the result of conductance, where we have also presented the polarization of the u_K branch defined by $P_K = [T_0 + \sum_{\mu=1}^{M}(T_\mu - T_{-\mu})]/(\sum_{\mu=-M}^{M} T_\mu)$. Note that when the Fermi energy lies between the zeroth and first modes of the u_K branch in the 1D ribbon, that is, $|m-\Delta| < E_F < \tau$, then only the channel of the zeroth mode, i.e., the flat band, can contribute to the conductance, see Fig. 4(b). Then, the conductance is quantized with $G = 1/h$, and only the u_K branch of the quasi-2D leads can be perfectly transmitted through the ribbon with the so-called valley polarization $P_K \simeq 1$. Note that in contrast to Ref. [32] where the valley is made out of a pseudospinor of graphene, this u_K valley carries the real spin freedoms of the spin-1/2 spinors.

As we show in Fig. 2, while the u_K branch of the leads transmit through the 1D zigzag ribbon, the corresponding topological and spin textures can be tuned by two external fields m and Δ simultaneously. When $m > \Delta$, we have $\mathcal{C}_{u_K} = -0.5$ and $s_z^K = 1/2$ at the K point. In this case, by adding an effective in-plane electric field along the ribbon [36], only the down spin of the u_K Dirac spinor can be transmitted, and it accumulates at the bottom of the right lead [lower shaded region in Fig. 4(a)] with half the unit spin Hall conductance $\sigma_{u_K}^s = 1/2h$. On the other hand, if m is tuned to be less than Δ, i.e., $m < \Delta$ such as $m = 0.13$, both the sign of Chern number $\mathcal{C}_{u_K}$ and direction of spin texture S_z^K would be reversed. Accordingly, we can let only the up spin of the u_K Dirac spinor transmit and accumulate at the other side of right lead [upper shaded region in Fig. 4 (a)]. Therefore, by tuning the parameter m, only the up- or down-spin freedom of the spin-1/2 spinors can transit through the zigzag ribbon.

Here we should mention that because there is no topological order in this system, the conductance quantization shown in Fig. 5 cannot be protected by topology. Therefore, the conductance quantization is sensitive to disorder. This is actually the case as that in graphene, for which the effect of disorder on the conductance quantization has been reviewed in [37]. Fortunately, for a mesoscopic system, such quantization and disorder damping have been experimentally observed in [38]. Therefore, we believe that the conductance quantization can also be detected in our system.

VII. DISCUSSION AND CONCLUSION

Finally, we discuss the experimental feasibility of actual realization of the system. First, there have been many proposals for the generation of hexagonal optical lattice. The simplest way is to superpose three coplanar traveling plane waves with the same field strength [4]. The three wave vectors form a trine: their sum vanishes and the angle between any two of them is $2\pi/3$. The optical potential is $v(\mathbf{r}) \propto 3 + 2\sum_{a=1}^{3}\cos(\mathbf{b}_a \cdot \mathbf{r})$ with $\mathbf{b}_{1(2)} = \frac{\sqrt{3}k_L(\mathbf{e}_x \mp \mathbf{e}_y)}{2}$ and $\mathbf{b}_3 = -\mathbf{b}_1 - \mathbf{b}_2$. Second, the staggered sublattice potential can be realized by breaking the reflection symmetry of the honeycomb potential. This can be implemented by superimposing three independent standing waves, and a phase φ is introduced by the replacement $\sum_{a=1}^{3}\cos(\mathbf{b}_a \cdot \mathbf{r}) \to \sum_{a=1}^{3}\cos(\mathbf{b}_a \cdot \mathbf{r} + \varphi)$. In this case, we have the staggered sublattice potential $m \propto |\varphi|$ [4]. Third, we may use laser methods to employ degenerate dark states in a four-level system with three levels coupled to a common

fourth, under pairwise two-photon-resonance conditions [39]. Such dressing fields can be applied to generate the Rashba type of non-Abelian gauge field for atoms trapped in optical lattices. Fourth, the polarization field Δ can be easily realized by introducing the population imbalance between two fermionic components. At first sight, it is a complicated task to implement all the optical lattice, the staggered sublattice potential m, the polarization field Δ, and the SOC simultaneously. Here we should mention that with the foreseeable advancement in the state of the art, we expect that the model can be realized in the foreseeable future. Finally, the accumulated up or down Dirac spinors in the right lead can be detected directly by spin-dependent imaging. Nevertheless, the atomic density may decrease away from the center of the trap because of the slowly varying trap potential. To solve this difficulty, we may consider a square-well potential with a sharp trap boundary [40,41]. Moreover, one may feel that because the narrow 1D ribbon of Fig. 4(a) is imprinted by using two lobes of a laser beam [34], the connection region between the 2D leads and 1D ribbon, i.e., the scatter region, may be irregular. To solve this problem, we have explored different configurations of the scatter region [42]. The results show that the conductances for different scatter regions are qualitatively the same. This would facilitate future experimental manipulations.

In conclusion, we have shown that the SO-coupled hexagonal lattice can give rise to a variety of spin-based physics of the spin-1/2 Dirac spinors in the marginal Abelian limit with $\kappa = \pi/2$. We investigate the spectrum of the 1D ribbons with different edges and calculate the conductances of the 1D zigzag ribbon with two quasi-2D leads. We show that only the spin-up or spin-down freedom of the Dirac spinors can transit through the zigzag ribbon by tuning the parameter m.

ACKNOWLEDGMENTS

We appreciate insightful discussions with A. H. Macdonald, who gave us many useful suggestions. This work is supported by the NCET, the NSFC under Grants No. 11074175, No. 10904096, No. 11204294, and No. 11274260, the NKBRSFC under Grant No. 2011CB921502, the General Research Fund of the Hong Kong Research Grants Council under Project No. CityU 100311/11P, and the City University of Hong Kong Research Project 9610180.

APPENDIX A: EFFECTIVE HAMILTONIAN AND EIGENVECTORS NEAR Γ AND K, K' POINTS

In the marginal Abelian regime with $\kappa = \pi/2$, we first derive the effective low-energy Hamiltonian for the Γ point, which reads

$$H_\Gamma = \begin{pmatrix} m+\Delta & 0 & 0 & \frac{3}{2}(k_x - ik_y) \\ 0 & m-\Delta & \frac{3}{2}(k_x + ik_y) & 0 \\ 0 & \frac{3}{2}(k_x - ik_y) & -m+\Delta & 0 \\ \frac{3}{2}(k_x + ik_y) & 0 & 0 & -m-\Delta \end{pmatrix}. \tag{A1}$$

By using the 4×4 matrices $\vec{\alpha} = \sigma_x \otimes \tau_i$ and $\beta = \sigma_z \otimes \hat{I}_\tau$, we can then derive Eq. (6).

The eigenvectors of H_Γ are four-component plane waves, which are given by

$$\begin{aligned} U_\Gamma &= \{u_1, u_2, u_3, u_4\} \\ &= \begin{pmatrix} \cos\frac{\theta_+}{2} e^{-i\varphi_{\vec{k}}} & 0 & 0 & -\sin\frac{\theta_+}{2} e^{-i\varphi_{\vec{k}}} \\ 0 & \cos\frac{\theta_-}{2} e^{i\varphi_{\vec{k}}} & -\sin\frac{\theta_-}{2} e^{i\varphi_{\vec{k}}} & 0 \\ 0 & \sin\frac{\theta_-}{2} & \cos\frac{\theta_-}{2} & 0 \\ \sin\frac{\theta_+}{2} & 0 & 0 & \cos\frac{\theta_+}{2} \end{pmatrix}. \end{aligned} \tag{A2}$$

Here, $\cos\theta_\pm = \frac{m\pm\Delta}{\sqrt{\frac{9}{4}k^2 + (m\pm\Delta)^2}}$ and $\varphi_{\vec{k}} = \arctan\frac{k_y}{k_x}$. The corresponding eigenenergies are $E_\Gamma = \pm\sqrt{\frac{9}{4}k^2 + (m\pm\Delta)^2}$. The two positive-energy spinors read $u_1 = (\cos\frac{\theta_+}{2} e^{-i\varphi_{\vec{k}}}, 0, 0, \sin\frac{\theta_+}{2})^T$ and $u_2 = (0, \cos\frac{\theta_-}{2} e^{i\varphi_{\vec{k}}}, \sin\frac{\theta_-}{2}, 0)^T$, which have opposite helicities.

While for the K and K' points, the corresponding effective Hamiltonians can be obtained as

$$H_K = \begin{pmatrix} m+\Delta & 0 & 0 & -2i \\ 0 & m-\Delta & -\frac{3}{2}(k_x - ik_y) & 0 \\ 0 & -\frac{3}{2}(k_x + ik_y) & -m+\Delta & 0 \\ 2i & 0 & 0 & -m-\Delta \end{pmatrix}, \tag{A3}$$

and

$$H_{K'}=\begin{pmatrix} m+\Delta & 0 & 0 & -\frac{3}{2}(k_x+ik_y) \\ 0 & m-\Delta & -2i & 0 \\ 0 & 2i & -m+\Delta & 0 \\ -\frac{3}{2}(k_x-ik_y) & 0 & 0 & -m-\Delta \end{pmatrix}. \tag{A4}$$

The eigenvectors of $H_{K(K')}$ read

$$U_K=\begin{pmatrix} 0 & 0 & 0 & 0 \\ 0 & \cos\frac{\theta_-}{2}e^{-i\varphi} & -\sin\frac{\theta_-}{2}e^{-i\varphi} & 0 \\ 0 & \sin\frac{\theta_-}{2} & \cos\frac{\theta_-}{2} & 0 \\ 0 & 0 & 0 & 0 \end{pmatrix}, \tag{A5}$$

and

$$U_{K'}=\begin{pmatrix} \cos\frac{\theta_+}{2}e^{i\varphi} & 0 & 0 & -\sin\frac{\theta_+}{2}e^{i\varphi} \\ 0 & 0 & 0 & 0 \\ 0 & 0 & 0 & 0 \\ \sin\frac{\theta_+}{2} & 0 & 0 & \cos\frac{\theta_+}{2} \end{pmatrix}, \tag{A6}$$

with the eigenenergies of nonzero eigenvectors given by $E_K=\pm\sqrt{\frac{9}{4}k^2+(m+\Delta)^2}$ and $E_{K'}=\pm\sqrt{\frac{9}{4}k^2+(m-\Delta)^2}$, respectively. The nonzero positive-energy eigenstates of $u_K=(0,\cos\frac{\theta_-}{2}e^{-i\varphi_{\vec{k}}},\sin\frac{\theta_-}{2},0)^T$ and $u_{K'}=(\cos\frac{\theta_+}{2}e^{i\varphi_{\vec{k}}},0,0,\sin\frac{\theta_+}{2})^T$ have the same eigenenergies as those of u_2 and u_1.

APPENDIX B: HOPPING MATRIX IN RIBBON HAMILTONIAN

In this Appendix, further information can be obtained by expressing the tight-binding Hamiltonian on the Bloch sums. The intracell and intercell hopping matrix for a zigzag ribbon are

$$T_z^{\text{intra}}=-2t\begin{pmatrix} \cos\kappa\cos\frac{\sqrt{3}k}{2} & i\sin\kappa\cos\left(\frac{\sqrt{3}k}{2}-\frac{\pi}{3}\right) \\ i\sin\kappa\cos\left(\frac{\sqrt{3}k}{2}+\frac{\pi}{3}\right) & \cos\kappa\cos\frac{\sqrt{3}k}{2} \end{pmatrix}, \quad T_z^{\text{inter}}=-t\begin{pmatrix} 2\cos\kappa & i\sin\kappa \\ i\sin\kappa & 2\cos\kappa \end{pmatrix}. \tag{B1}$$

And for an armchair ribbon,

$$T_a^{\text{intra}}=t\begin{pmatrix} -\cos\kappa e^{-ik} & i\sin\kappa e^{-ik} \\ i\sin\kappa e^{-ik} & -\cos\kappa e^{-ik} \end{pmatrix}, \quad T_a^{\text{inter}}=t\begin{pmatrix} -\cos\kappa e^{-i\frac{k}{2}} & i\sin\kappa e^{-i(\frac{k}{2}-\frac{\pi}{3})} \\ i\sin\kappa e^{-i(\frac{k}{2}+\frac{\pi}{3})} & -\cos\kappa e^{-i\frac{k}{2}} \end{pmatrix}. \tag{B2}$$

[1] M. Lewenstein, A. Sanpera, V. Ahufinger, B. Damski, A. Sen De, and U. Sen, Adv. Phys. **56**, 243 (2007).

[2] S.-L. Zhu, B.-G. Wang, and L.-M. Duan, Phys. Rev. Lett. **98**, 260402 (2007).

[3] B. Wunsch, F. Guinea, and F. Sols, New J. Phys. **10**, 103027 (2008).

[4] K. L. Lee, B. Grémaud, R. Han, B. G. Englert, and C. Miniatura, Phys. Rev. A **80**, 043411 (2009).

[5] P. Soltan-Panahi, J. Struck, P. Hauke, A. Bick, W. Plenkers, G. Meineke, C. Becker, P. Windpassinger, M. Lewenstein, and K. Sengstock, Nat. Phys. **7**, 434 (2011).

[6] L. Tarruell, D. Greif, T. Uehlinger, G. Jotzu, and T. Esslinger, Nature **483**, 302 (2012).

[7] A. H. Castro Neto, F. Guinea, N. M. R. Peres, K. S. Novoselov, and A. K. Geim, Rev. Mod. Phys. **81**, 109 (2009).

[8] M. Hasan and C. Kane, Rev. Mod. Phys. **82**, 3045 (2010).

[9] X.-L. Qi and S.-C. Zhang, Rev. Mod. Phys. **83**, 1057 (2011).

[10] S. A. Wolf, D. D. Awschalom, R. A. Buhrman, J. M. Daughton, S. V. Molnár, M. L. Roukes, A. Y. Chtchelkanova, and D. M. Treger, Science **294**, 1488 (2001).

[11] I. Žutić, J. Fabian, and S. Das Sarma, Rev. Mod. Phys. **76**, 323 (2004).

[12] J. Dalibard, F. Gerbier, G. Juzeliūnas, and P. Öhberg, Rev. Mod. Phys. **83**, 1523 (2011).

[13] Y.-J. Lin, K. Jiménez-García, and I. B. Spielman, Nature **471**, 83 (2011).

[14] P.-J. Wang, Z.-Q. Yu, Z.-K. Fu, J. Miao, L.-H. Huang, S.-J. Chai, H. Zhai, and J. Zhang, Phys. Rev. Lett. **109**, 095301 (2012).

[15] L. W. Cheuk, A. T. Sommer, Z. Hadzibabic, T. Yefsah, W. S. Bakr, and M. W. Zwierlein, Phys. Rev. Lett. **109**, 095302 (2012).
[16] N. Goldman, A. Kubasiak, A. Bermudez, P. Gaspard, M. Lewenstein, and M. A. Martin-Delgado, Phys. Rev. Lett. **103**, 035301 (2009).
[17] W. S. Cole, S. Z. Zhang, A. Paramekanti, and N. Trivedi, Phys. Rev. Lett. **109**, 085302 (2012).
[18] J. Radić, A. DiCiolo, K. Sun, and V. Galitski, Phys. Rev. Lett. **109**, 085303 (2012).
[19] A. Bermudez, N. Goldman, A. Kubasiak, M. Lewenstein, and M. A. Martin-Delgado, New J. Phys. **12**, 033041 (2010).
[20] N. Goldman, I. Satija, P. Nikolic, A. Bermudez, M. A. Martin-Delgado, M. Lewenstein, and I. B. Spielman, Phys. Rev. Lett. **105**, 255302 (2010).
[21] A. Bermudez, L. Mazza, M. Rizzi, N. Goldman, M. Lewenstein, and M. A. Martin-Delgado, Phys. Rev. Lett. **105**, 190404 (2010).
[22] U. Schneider *et al*., Nat. Phys. **8**, 213 (2011).
[23] G. W. Semenoff, Phys. Rev. Lett. **53**, 2449 (1984).
[24] P. A. M. Dirac, Proc. Roy. Soc. A **117**, 610 (1928).
[25] Z. Lan, N. Goldman, A. Bermudez, W. Lu, and P. Öhberg, Phys. Rev. B **84**, 165115 (2011).
[26] Z. Lan, N. Goldman, and P. Öhberg, Phys. Rev. B **85**, 155451 (2012).
[27] F. D. M. Haldane, Phys. Rev. Lett. **61**, 2015 (1988).
[28] B. A. Bernevig, T. L. Hughes, and S. C. Zhang, Science **314**, 1757 (2006).
[29] K. Nakada, M. Fujita, G. Dresselhaus, and M. S. Dresselhaus, Phys. Rev. B **54**, 17954 (1996).
[30] L. Brey and H. A. Fertig, Phys. Rev. B **73**, 235411 (2006).
[31] N. M. R. Peres, A. H. Castro Neto, and F. Guinea, Phys. Rev. B **73**, 195411 (2006).
[32] A. Rycerz, J. Tworzydło, and C. W. J. Beenakker, Nat. Phys. **3**, 172 (2007).
[33] A. Sommer, M. Ku, G. Roati, and M. W. Zwierlein, Nature **472**, 201 (2011).
[34] J. P. Brantut, J. Meineke, D. Stadler, S. Krinner, and T. Esslinger, Science **337**, 1069 (2012).
[35] T. Ando, Phys. Rev. B **44**, 8017 (1991).
[36] Y.-J. Lin, R. L. Compton, K. Jimenez-Garcia, W. D. Phillips, J. V. Porto, and I. B. Spielman, Nat. Phys. **7**, 531 (2011).
[37] A. Cresti, N. Nemec, B. Biel, G. Niebler, F. Triozon, G. Cuniberti, and S. Roche, Nano Res **1**, 361 (2008).
[38] Y.-M. Lin, V. Perebeinos, Z. Chen, and P. Avouris, Phys. Rev. B **78**, 161409 (2008).
[39] J. Ruseckas, G. Juzeliūnas, P. Öhberg, and M. Fleischhauer, Phys. Rev. Lett. **95**, 010404 (2005).
[40] A. L. Gaunt, T. F. Schmidutz, I. Gotlibovych, R. P. Smith, and Z. Hadzibabic, Phys. Rev. Lett. **110**, 200406 (2013).
[41] K. Sun, W. V. Liu, A. Hemmerich, and S. Das Sarma, Nat. Phys. **8**, 67 (2012).
[42] K. Wakabayashi, Phys. Rev. B **64**, 125428 (2001).